Impact of domains on the orthorhombic-tetragonal transition of $BaTiO_3$: An *ab initio* study

Anna Grünebohm [1] and Madhura Marathe [2,3]

[1] *Interdisciplinary Centre for Advanced Materials Simulation (ICAMS), Ruhr-University Bochum, 44780 Bochum, Germany*
[2] *Institut de Ciència de Materials de Barcelona (ICMAB-CSIC), Campus UAB, 08193 Bellaterra, Spain*
[3] *Universitat Autònoma de Barcelona, 08193 Bellaterra, Spain*

(Received 24 September 2020; accepted 5 November 2020; published 23 November 2020)

We investigate the multidomain structures in the tetragonal and orthorhombic phases of $BaTiO_3$ and the impact of the presence of domain walls on the intermediary phase transition. We focus on the change in the transition temperatures resulting from various types of domain walls and their coupling with an external electric field. We employ molecular dynamics simulations of an *ab initio* effective Hamiltonian in this study. After confirming that this model is applicable to multidomain configurations, we show that the phase-transition temperatures strongly depend on the presence of domains walls. Notably we show that elastic 90° walls can strongly reduce thermal hysteresis. Further analysis shows that the change in transition temperatures can be attributed to two main factors: long-range monoclinic distortions induced by walls within domains and domain wall widths. We also show that the coupling with the field further facilitates the reduction of thermal hysteresis for orthorhombic 90° walls, making this configuration attractive for future applications.

DOI: 10.1103/PhysRevMaterials.4.114417

I. INTRODUCTION

In the last decades the functional properties of ferroelectric (FE) perovskites came into focus for exciting applications [1]. In particular, Pb-free $BaTiO_3$-based materials are promising for sustainable technologies with operating temperatures at and below room temperature [2]. $BaTiO_3$ (BTO) crystallizes in the paraelectric (PE) cubic phase ($Pm\bar{3}m$) at high temperatures, and below 120°C, 5°C, and −80°C the FE tetragonal (T), orthorhombic (O) and rhombohedral (R) phases with $P4mm$, $Amm2$, and $R3m$ symmetry occur [3–5]. For applications close to ambient temperatures thus in particular the T and O ferroelectric phases and the transition between them are relevant. There are only a few reports which have studied the T-O transition in detail [4–8]. X-ray diffraction measurements have pointed to the existence of an intermediate phase with short-range monoclinic order at this transition [7,9] and under an applied field the T phase transforms to a monoclinic phase which remains stable after removing the field [10]. Another measurement also confirmed the existence of monoclinic phases and reported a "thermotropic" phase boundary [11], which is the temperature analog of concentration-dependent morphotropic phase boundaries. Such phase boundaries are related to flat energy landscapes, enhanced polarization rotation, and in turn exceptionally large functional responses [12,13].

The T-O transition is a first-order phase transition with phase coexistence and a broad thermal hysteresis between the transition temperatures for cooling (T_C^c) and heating (T_C^h) [3]. Furthermore, the different nature of the phase transition with abrupt versus continuous changes in polarization while cooling and heating has been reported [4,14]. The measured transition temperatures for the T-O transition have a large error bar of more than 10 K which is comparable to the magnitude of the hysteresis itself [4–7,14]. Hysteresis potentially results in reduced reversible functional responses and a wide range of responses for different samples, making the material unsuitable for devices which require long operational lifetime [15,16]. Therefore, it is important to understand the extrinsic and intrinsic factors which contribute to thermal hysteresis and the order of the transition. So far, the large error bars in T_C's have been attributed to the presence of domains [4,14]. Domains and domain walls are also known as one of the major sources of extrinsic functional responses [17]. Furthermore, recent developments in the field of sample preparation and measurement techniques with atomic resolution bring the idea of engineered domain walls (DWs) within our reach and allow us to master hysteresis by microstructure design. Domain engineering designed for specific applications [18,19] and optimization of functional responses [20–22] has already been tested in experiments. Therefore, in the present study, we focus on domains and how the presence of multidomain (MD) phases affects T_C, the nature of phase transition, and its thermal hysteresis.

As dictated by underlying crystal symmetry, polarization $\boldsymbol{P}$ along all ⟨100⟩ and ⟨110⟩ directions would lead to degenerate states for T and O phases, respectively. The single-domain (SD) system with polarization along any one of these directions would be the ground state for ideal materials under perfect screening. However, typically multidomain phases are prevalent in which domains of different polarization directions coexist and are separated by a domain wall in which the polarization changes direction. These walls are characterized by the angle of the polarization rotation along the domain wall normal, e.g., 180° between domains with $\pm\boldsymbol{P}$ along [010] or [011], respectively. Possible reasons for the stability of

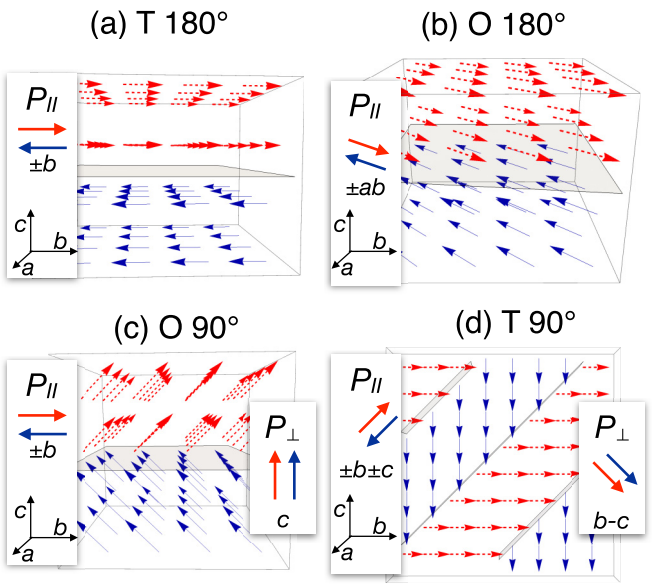

FIG. 1. Local dipole configurations of the T and O phases of $BaTiO_3$ under study: (a, b) nonelastic 180° DWs and (c, d) elastic 90° DWs. Insets illustrate the polarization component parallel to the wall ($P_{||}$) (a,c) along [010], i.e., along $\pm b$, (b) along [110] and (d) along [011] and the component perpendicular to elastic walls ($P_{\perp}$) (c) along [001], i.e. along c and (d) [110]. For 180° walls, $P_{\perp}$ is along [001].

domain walls include local strain [23], the presence of defects [24], and depolarization fields [25]. Furthermore, domains may nucleate in the course of the heat treatment which are at least metastable afterwards [20,26].

So far the understanding of the coupling of domain structure and the T-O transition is only rudimentary. Piezoresponse force microscopy has been used to image domain patterns within the T and O phases as well as evolution of domains at the phase transition [4,6]. In general, it is, however, challenging to visualize and interpret the complex domain structures especially near phase transitions and to disentangle the impact of superposition of various DWs and their interactions, defects, and inhomogeneities in the real sample. Theoretical simulations provide an ideal tool to separate the different elements of the microstructure by considering an "idealized" system. However, previous theoretical studies have focused on the domain structure of the T or O phase either using density functional theory simulations at 0 K [27,28] or phenomenological models [29,30] away from the phase transition. Moreover, when the phase transition has been studied the impact of domains is usually neglected [31,32].

In the present paper, we close this gap by a systematic study of the T-O transition in the presence of domains focusing on specific low-energy configurations which are most common in experimental studies, namely, planar charge-neutral 90° and 180° walls along high-symmetry directions [4]. In nonelastic 180° walls, the same strain occurs in adjacent domains [shown in Figs. 1(a) and 1(b)], whereas the considered 90° DWs [Figs. 1(c) and 1(d)] are elastic. These walls are aligned along ⟨100⟩ and ⟨110⟩ in the O and T phases, respectively. Note that the alignment of 180° walls is not fully

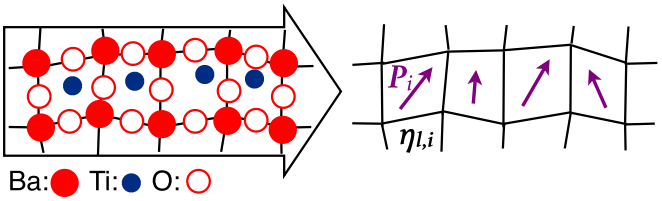

FIG. 2. Illustration of the used coarse-grained model: the electronic and atomic degrees of freedom are mapped on the local dipole moment $\boldsymbol{u}_i$, i.e., the local polarization $\boldsymbol{P}_i$ and the local strain $\boldsymbol{\eta}_{l,i}$.

determined by symmetry (e.g., for P_b and P_{-b}, all walls parallel to [001] are analogous to nonelastic charge-neutral walls); however, we focus only on the limiting cases being along the crystallographic ⟨100⟩ directions. Previous theoretical works [29,33] have shown that these directions are favorable.

For potential applications, not only thermal hysteresis and character of the transition but also their coupling to an external field is relevant and would determine the functional properties. For example, it has been discussed in the literature that giant caloric and piezoelectric responses are possible for a field-induced phase transition [2,22,34,35]. Therefore, we study the effect of an applied field on the evolution of multidomain phases as a function of temperature as well as the density of domain walls. Our main aims are to understand the properties of MD phases around and at the T-O phase transition and to explore possibilities to engineer these phases to reduce the thermal hysteresis.

The paper is organized as follows: the used *ab initio*–based method and simulation details are summarized in Sec. II, our results describing the properties of domain walls in T and O phases and the interplay between domain structure and the phase transition are discussed in Sec. III, and finally conclusions and outlook are given in Sec. IV.

II. COMPUTATIONAL DETAILS

We employ the effective Hamiltonian [36,37] defined for cubic perovskite ferroelectrics. Instead of treating all atomic positions as degrees of freedom, the collective atomic displacements are coarse grained by local soft mode vectors $\boldsymbol{u}_i$ and local acoustic displacement vectors $\boldsymbol{w}_i$ of each unit cell i in the simulation supercell. An internal optimization of $E(\boldsymbol{w}_i)$ is used, reducing the degrees of freedom per formula unit from five atoms times the three Cartesian directions (= 15) to the three components of the soft mode $\boldsymbol{u}_i$ corresponding to the local polarization $\boldsymbol{P}_i$ (see Fig. 2). This method has been used extensively to study various properties such as phase diagrams [32,38,39], domain structures [23,40,41], and functional responses [42–44] of ferroelectric materials.

The effective Hamiltonian [36,37] is written as follows:

$$
\begin{aligned}
H^{\text{eff}} = {} & \frac{M^*_{\text{dipole}}}{2} \sum_{i,\alpha} \dot{u}^2_{\alpha,i} \\
& + V^{\text{self}}(\{\boldsymbol{u}\}) + V^{\text{dpl}}(\{\boldsymbol{u}\}) + V^{\text{short}}(\{\boldsymbol{u}\}) \\
& + V^{\text{elas, homo}}(\eta_1, \ldots, \eta_6) + V^{\text{elas, inho}}(\{\boldsymbol{w}\}) \\
& + V^{\text{coup, homo}}(\{\boldsymbol{u}\}, \eta_1, \ldots, \eta_6) + V^{\text{coup, inho}}(\{\boldsymbol{u}\}, \{\boldsymbol{w}\}),
\end{aligned}
\tag{1}
$$

with $\eta_1, \ldots, \eta_6$ being the six components of homogeneous strain in Voigt notation. The first term represents the kinetic energies of the local soft modes while M^*_{dipole} corresponds to the effective mass. Furthermore, $V^{\text{self}}(\{\boldsymbol{u}\})$ is the self-energy of the local mode, $V^{\text{dpl}}(\{\boldsymbol{u}\})$ is the long-range dipole-dipole interaction, $V^{\text{short}}(\{\boldsymbol{u}\})$ is the short-range interaction between local soft modes, $V^{\text{elas, homo}}(\eta_1, \ldots, \eta_6)$ is the elastic energy from homogeneous strains, $V^{\text{elas, inho}}(\{\boldsymbol{w}\})$ is the elastic energy from inhomogeneous strains, $V^{\text{coup, homo}}(\{\boldsymbol{u}\}, \eta_1, \ldots, \eta_6)$ is the coupling between the local soft modes and the homogeneous strain, and $V^{\text{coup, inho}}(\{\boldsymbol{u}\}, \{\boldsymbol{w}\})$ is the coupling between the soft modes and the inhomogeneous strains. The coupling with an external electric field $-Z^*\boldsymbol{E}_i \cdot \boldsymbol{u}_i$ is also included in the Hamiltonian, where Z^* is the Born effective charge associated with the soft mode. The set of parameters for $BaTiO_3$ has been obtained using density functional theory simulation and is listed in Ref. [45].

Molecular dynamics simulations are performed by employing the FERAM code [46] developed by Nishimatsu *et al.* [47]. The Nosé-Poincaré thermostat [48] is used to simulate annealing starting well apart from the transition temperatures of our model. At each T, after 120.000 fs thermalization, the local dipoles $\boldsymbol{P}_i$ are averaged over 160.000 fs and the final configuration is used to restart the next T step. We use temperature sweep rates of up to 2×10^5 K/s, and 5-K steps. At each T, the energy and the local polarization $\boldsymbol{P}_i$ allow us to determine the phase. Although the symmetry of the sample may be reduced by domains, we speak of T and O phases if the system apart from domain walls has local polarization $P_{\langle 100\rangle}$ or $P_{\langle 110\rangle}$, respectively. We also use T and O to characterize phases with small field-induced monoclinic distortions; e.g., $0 < P_{[010]} \ll P_{[001]}$ is called T.

In experiments, nucleation of different domains is observed at phase boundaries which can also be found in our simulations. However, recall that in simulations, the material is under "ideal" conditions, i.e., absence of inhomogeneities and depolarization effects as well as there being finite size effects; therefore, the probability of nucleation of domain walls is much smaller than that in experiments [49]. Furthermore, we want to understand the effects of different types of domain walls separately, which would not be possible for randomly nucleated structures. Therefore, we initialize our system with a well-defined local dipole arrangement at a temperature well away from the phase boundaries. This allows us to study properties of a desired "geometry," i.e., orientation and size of domains for a multidomain phase without any additional effects. For this purpose we use a supercell size of $96 \times 96 \times 96$ formula units being equivalent to a sample of about $38 \times 38 \times 38$ nm^3 with periodic boundary conditions. We initialize equally spaced domain walls with distances of $d = 19.1$, 9.6, and 4.8 nm which correspond to presence of two, four, and eight DWs in the supercell, respectively. For 90° walls in the O phase, we have furthermore considered $d = 23.9$ nm and $d = 12$ nm using two and four domains in combination with a $96 \times 96 \times 120$ supercell. For 90° walls in the T phase, we restrict our study to the minimal number of four walls with $d = 13.5$ nm compatible with the periodic boundary conditions for these walls along [110]. The number of domain walls considered here for each structure is determined by the periodic boundary conditions and the size of the supercell.

III. RESULTS AND DISCUSSION

A. Characterization of MD configurations

As a starting point, we characterize multidomain configurations in both tetragonal and orthorhombic phases separately using supercells with well-defined domain wall distances as described in Sec. II [50]. We project the polarization on the two components (i) parallel ($P_{||}$) and (ii) perpendicular ($P_\perp$) to the wall; these directions are defined for each configuration in Fig. 1. We plot these two components for various MD configurations in Fig. 3. For the studied charge-neutral walls, $P_\perp$ is constant across the domain walls as illustrated by dashed lines, with $P_\perp = P_{[001]}$ at the O90° wall [see Fig. 3(a)], zero across nonelastic walls such as O180° [as shown in Fig. 3(b)], and $P_\perp = P_{[110]}$ at the T90° wall [see Fig. 3(c)]. We do not find any significant change in $P_\perp$ for O90 and O180 walls; however, for T90 walls, it increases as temperature is reduced towards the transition temperature. The parallel component $P_{||}$ reverses the sign across the DW for all the configurations. This is expected based on underlying symmetries for the MD phases. $P_{||}$ approximately follows a tanh profile as previously discussed in the literature [27,29,51,52] and decreases if the system approaches T_C in the presence of elastic walls. We estimate the domain wall widths $2d_{\text{DW}}$ by fitting the polarization profile across a single wall with

$$P_{||}(z) = P_{0,||}(z_0) \tanh\left[\frac{(z - z_0)}{d_{\text{DW}}}\right], \tag{2}$$

as shown with solid lines in Fig. 3. Here $z - z_0$ corresponds to the distance from the center of the wall.

The calculated DW width is plotted in Fig. 4 for different types of walls. We find that T90 walls are thickest, followed by O90 and O180 walls, and the T180 walls are the narrowest among those under study. This trend compares well with those results obtained from the Ginzburg-Landau-Devonshire model [29] and density functional theory [27]. Note that no quantitative agreement may be expected due to the different approximations such as dependence on the parametrization of the first and zero-temperature results of the second method; furthermore, our polarization data have a resolution of 0.4 nm. We reproduce the findings in Ref. [53] that the walls occasionally shift via a transient state with broadened domain walls. Furthermore, we observe the predicted increase of d_{DW} with increasing temperature [29]. For 180° walls, the temperature dependence of d_{DW} is weaker compared to 90° walls and a large broadening occurs near the transition temperature for the latter. The broadening of the walls is related to fluctuations of the dipoles in the domain walls which strongly increase close to the transition temperature. Moreover, we observe a considerable broadening of T180 and T90 walls at high temperatures as the system approaches the ferroelectric-to-paraelectric transition temperature due to large fluctuations associated with this transition. The observation of domain wall broadening close to T_C goes beyond predictions by Ginzburg-Landau theory [29] probably because the fluctuations of the order parameter are not fully included in that method.

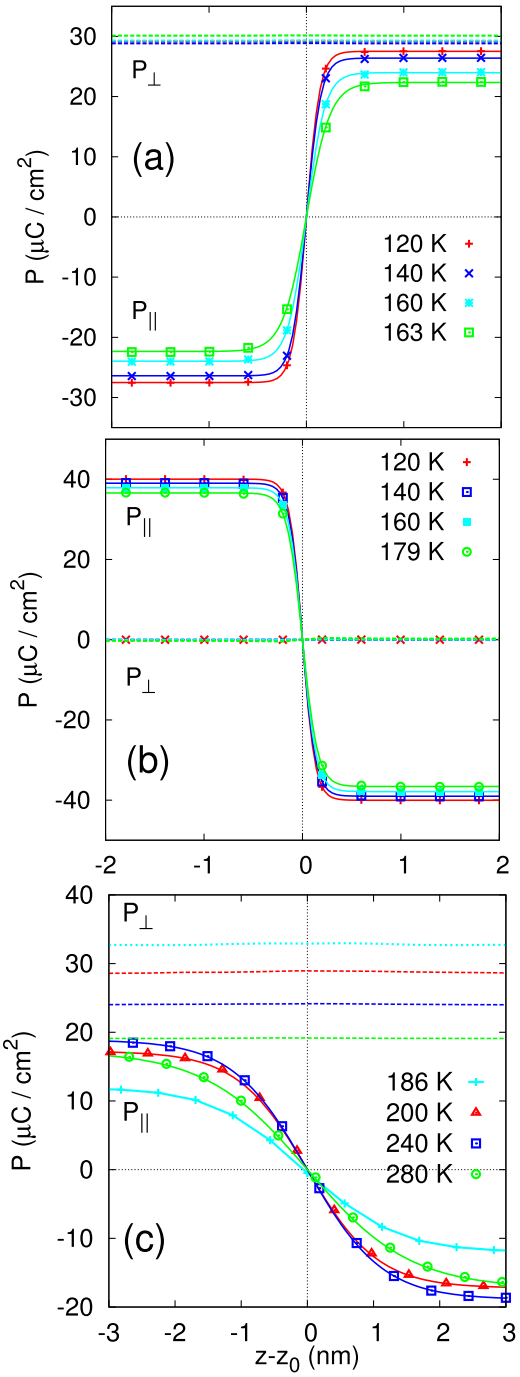

FIG. 3. Average polarization per layer $\langle P_i \rangle_c (z - z_0)$ across (a) O90, (b) O180, and (c) T90 domain walls. Symbols correspond to simulated $P_{||}$, solid lines to tanh fit [Eq. (2)] and dashed lines to $P_\perp$. Here z_0 corresponds to the center of the DW. We note that T_C for configurations (a), (b), and (c) correspond to 163, 179, and 184 K, respectively (discussed later in detail).

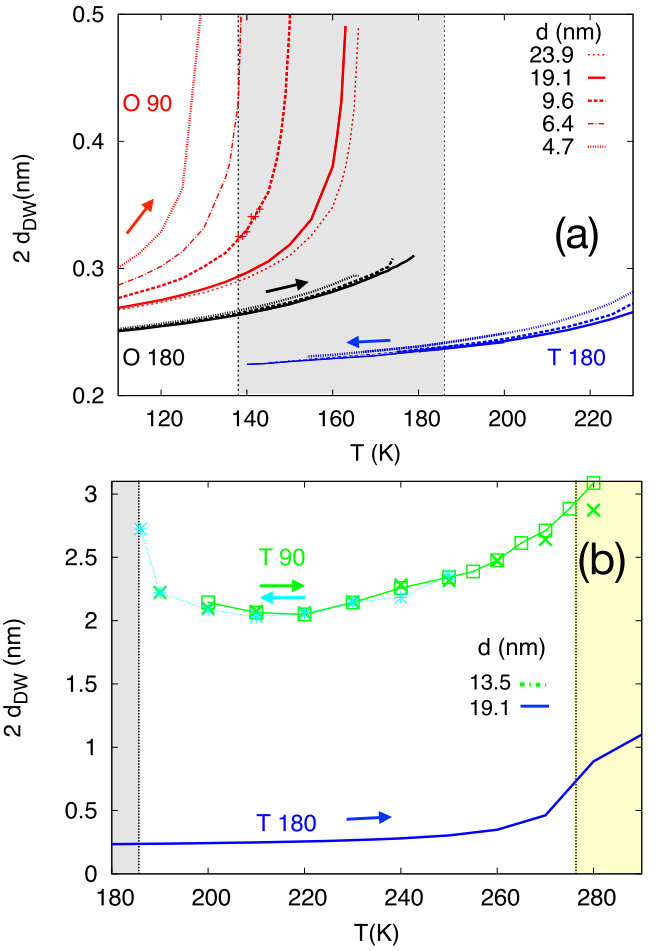

FIG. 4. Temperature dependence of $2d_{DW}$ for O90 (red), O180 (black), T180 (blue), and T90 (green/cyan) walls (a) approaching the T-O transition and (b) in the whole T phase. Line types mark the wall distances d and the direction of arrows illustrates the direction of temperature change (i.e., heating and cooling simulations). For three examples also results for cooling simulations have been added (symbols). The coexistence ranges for the T-O and T-C transitions without domains are highlighted in gray and yellow, respectively.

The domain density does not affect the DW width even for minimal distances of 4.8 nm. It is further important to note that we obtain the same widths during the heating and cooling simulations as illustrated by symbols for some exemplary configurations in Fig. 4. Thus this property is a material property at any temperature and is not influenced by thermal history, changes of domain wall positions, etc. Along with this analysis of local polarization and DW widths, we also examined the energies of the MD configurations for different wall densities and temperatures. We find total energy penalties of 7, 13, and 14 $\mathrm{mJ/m^2}$ for O90, T180, and O180 walls (for $d = 19.1$ nm and at 120 K for the O phases and 220 K for the T phase) in qualitative agreement to 4, 6, and 9 $\mathrm{mJ/m^2}$ found for their free energies with Landau theory [29] and values of 6-14 $\mathrm{mJ/m^2}$ for T180 walls reported at 0 K based on density functional theory [27]. However, we could not do any systematic convergence tests for the T90 walls with respect to d and expect slow convergence due to the large distortions of the domains (discussed later). For this configuration, the calculated energy penalty of 4 $\mathrm{mJ/m^2}$ at 220 K is smaller than previously reported values. For all other walls, the domain wall profiles and energies are converged with respect to the system size. From this analysis, we conclude that these MD configurations are well described within our model and simulation cell size.

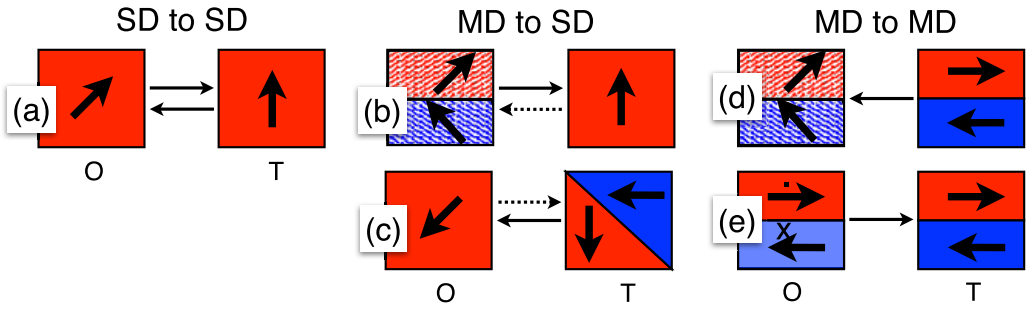

FIG. 5. Schematic pictures of the observed changes of domain structure at the T-O transition: (a) SD O ⇆ SD T, e.g., between bc and c; (b) O90 ⇆ SD T, e.g., $bc/-bc$ to c; (c) T90 ⇆ O SD, e.g., between b/c and bc; (d) T 180° → O90°, e.g., from $b/-b$ to $bc/-bc$; and (e) O180 → T180, e.g., $ab/-a-b$ to $b/-b$. Note that in (e) dots and crosses mark polarization out of plane and in plane, respectively. Arrows between two phases indicate transitions which are observed commonly (solid) and only occasionally due to nucleation (dotted).

B. Effect of domains on T_C

We now turn to the main focus of our work: How do the domains evolve near the transition and what is their impact on the transitions? In absence of domains and external field, we observe a sharp first-order transition with a jump of order parameter and energy at the transition temperature. Our calculated transition temperatures are $T_C^c = 138$ K for cooling and $T_C^h = 186$ K for heating; that is, we get a thermal hysteresis of about 50 K. The quantitative disagreement with experimental data is expected as the used model systematically underestimates transition temperatures and as the thermal hysteresis is considerably higher in an ideal material [32].

In the presence of domains, we observe different types of transitions between SD and MD phases which are summarized in Fig. 5. In all cases, the walls do not disperse during the phase transition and the local polarization rotates by 45° analogous to the SD case shown in Fig. 5(a). This results in two different scenarios: (1) for 90° walls, the polarization in both domains rotates to the initial $P_\perp$ direction and transforms to the SD phase [Figs. 5(b) and 5(c)], and (2) for 180° walls, no such rotation is possible and we observe T180-to-O90 and O180-to-T180 transitions [see Figs. 5(d) and 5(e)]. We note that the first-order character of this phase transition persists in the presence of domains walls, and we observe an abrupt transition with a jump in energy and polarization for all the systems considered. Occasionally, multidomain phases nucleate near the transition even for initial SD phases, as illustrated by dashed arrows in Fig. 5. However, we do not discuss these transitions here as the probability of such nucleation is rather low in our simulations.

Transition temperatures in the presence of domain walls are plotted as a function of wall densities in Fig. 6 [54]. Domains generally promote the phase transition and thus reduce T_C^h and enhance T_C^c as compared to the SD phase. For 180° walls, T_C converges slowly towards the SD phase boundaries with increasing wall distances; therefore, when starting with O-MD phases T_C^h increases with d while for T-MD phases T_C^c decreases. The convergence towards the SD phase boundary is generally expected because with decreasing DW density (equivalently increasing d) the volume fraction of dipoles near a DW as well as potential interactions between walls decrease. For O90 walls, the change of T_C with the wall distances is considerably smaller. Note that for the densest DW considered within our study, the MD phases are not stable in the vicinity of the phase transition and the system transforms to the SD phase (that is, O-MD to O-SD and T-MD to T-SD phases) at a temperature T_t (indicated in blue in Fig. 6).

The change in the transition temperatures is larger for 90° walls than for 180° walls. For example, heating from the O phase at $d = 9.6$ nm, we observe $T_C^h = 174$ K for O180 and 151 K for O90 walls, respectively. While cooling down from the T-MD phases, the increase of T_C^c by T180 walls is small (green crosses), whereas we observe a reduction of the thermal hysteresis to only 2 K in the presence of T90 walls with $d = 13.5$ nm [55].

To analyze the impact of domains on T_C, one may distinguish between rotation of polarization and strain variation

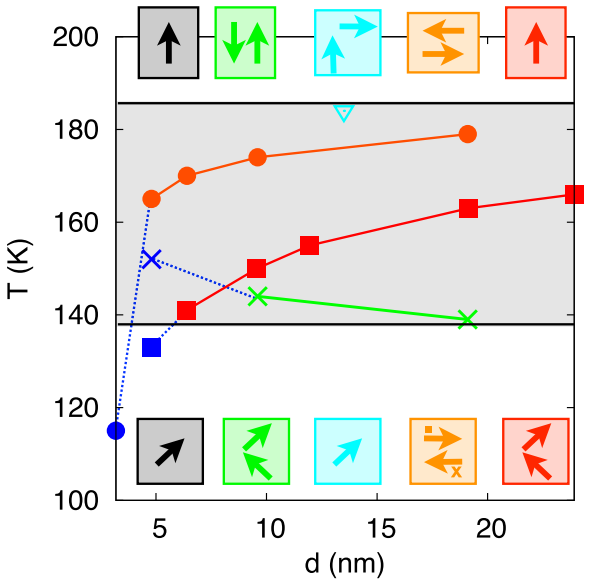

FIG. 6. Transition temperatures without external field as a function of the domain wall distance for transitions O90 → T-SD (red squares), T180 → O90 (green crosses), O180 → T180 (orange circles), and T90 → O-SD (cyan triangle). These transitions are illustrated in the insets. For dense walls, blue symbols mark temperatures T_t at which the MD configuration transforms to the ground-state SD configuration without any phase transition. The gray shaded area illustrates the coexistence range for T-SD to O-SD transition.

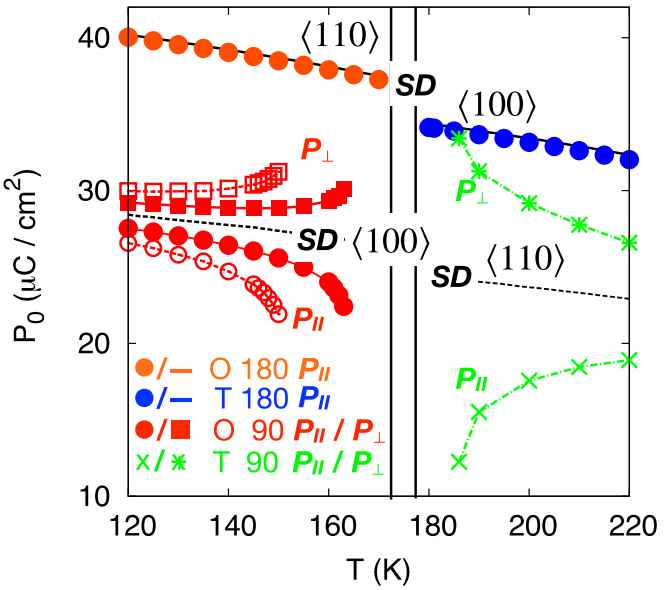

FIG. 7. Projections of polarization parallel and perpendicular to the wall ($P_{||,0}$ and $P_{\perp,0}$) in the center of O90 (red) for $d = 19.1$ nm (solid lines) and 9.6 nm (dashed lines); O180 (orange) for $d = 19.1$ nm; T180 (blue) for $d = 19.1$ nm; and T90 (green) for $d = 13.5$ nm configurations. Here we excluded regions near phase transitions. $P_{||,0}$ has been determined by Eq. (2) and $P_{\perp,0}$ corresponds to the sample average. As a reference, SD results projected on the same directions are added in black.

observed in the domains ("volume effect") and the properties of domain walls themselves ("interface effect"). To examine the volume effect, we look at the changes in polarization at the center of the domains where the effects arising from the interfaces themselves, i.e., the domain walls, should be minimal. For this purpose, we calculate the polarization in the center of the domain $P_{||,0}$ using Eq. (2). The resulting polarization in the domain centers is plotted in Fig. 7 as a function of temperature. In the case of 180° walls, the $P_{||}$ component matches exactly to the magnitude of the overall polarization of the SD phases and $P_\perp$ is equal to zero. The impact of temperature on the polarization direction in both domains is negligible. Thus, 180° DWs have no impact on the local polarization in the adjacent domains. In the case of O90° walls, $P_\perp$ and $P_{||}$ both correspond to ⟨100⟩ directions. Thus, if domain walls had no impact on the local polarization in the domain center, one would expect $P_\perp = P_{||}$ as $P = P_\perp + P_{||}$ would point along the ⟨[110]⟩ direction of a particular orthorhombic variant. In contrast to that we observe a monoclinic distortion of the polarization with $P_{\perp,0} > P_{||,0}$ (cf. red squares and red circles in Fig. 7). The monoclinic distortion is even larger in the case of the T90 wall for which the $P_\perp$ and $P_{||}$ both correspond to ⟨110⟩ directions (cf. green stars and crosses). Away from phase transitions, the monoclinic distortion increases with the domain wall density. The considerable monoclinic distortion even in the center of domains shows that the elastic walls induce long-range modification in the system both in polarization and strain. This explains much slower convergence of T_C with respect to d for O90 walls compared to other configurations.

Approaching the transition temperatures, i.e., heating O90 or cooling T90 configurations, the monoclinic distortions increase for MD configurations. Enhanced monoclinic distortions close to ferroelectric-ferroelectric transitions can be related to reduced anisotropy energy and energy penalty of reorientation of dipoles near the phase boundary and allow for monoclinic bridging phases which have been discussed earlier [56,57]. Such a monoclinic bridging state generally reduces the energy barrier between different phases promoting the phase transition. The changes in T_C in our study are related to the size of the monoclinic distortion and indeed the largest change observed for the T90 configuration corresponds to the largest distortion obtained in our study.

Second, to examine the interface effects, we look at the properties of domains walls themselves. As discussed earlier (Fig. 4 and subsequent discussion), the 180° walls are extremely thin and their width does not diverge even in the vicinity of the phase transition, whereas the elastic walls are slightly wider and diverge as the system approaches transition. Furthermore, 180° walls are Ising-like, i.e., the polarization in the center of the wall does not point along the polarization direction of either domain but rather decreases in magnitude only. However, for the O90 wall, the polarization in the center of the wall is pointing along ⟨100⟩ (i.e., along the spontaneous polarization of the T phase), and for the T90 wall, along ⟨110⟩ (i.e., along the spontaneous polarization of the O phase) and may thus act as nucleation centers for the transition. Thus for 90° walls, both volume and interface effects come together to accelerate the phase transition, whereas for 180° walls, only interface effects contribute to the change in T_C.

Interestingly, the same trends also occur at the orthorhombic-to-rhombohedral transition where both O90 and O180 phases transform to R109 configurations with $[\pm 1 \pm 11]$ domains and with $P_{||} < P_\perp$ similar to the O90 case. Similar to the discussion on the T-O transition, T_C is enhanced by only 5–10 K and at the same time, there are no considerable monoclinic distortions in the initial O phase. This points to the general trend that the long-range monoclinic distortions induced by elastic walls are important to modify T_C. However, a detailed study of this transition is out of scope for this paper.

C. Coupling of electric field and MD phases

Next, to shed light on the DW-field coupling, we performed cooling and heating simulations in the presence of an external field along ⟨100⟩. Recall that for MD phases, the relative orientation between the field and local polarization in each domain may be different, and the direction of the field relative to the DW also influences the field coupling. Unless specified otherwise, we applied the field parallel to the DW [58].

The calculated transition temperatures are plotted in Fig. 8 as a function of applied field magnitude at several d. The shifts in T_C's with respect to d which already have been discussed in Fig. 6 are not affected by an application of the field. For SD phases, both T_C^c and T_C^h reduce systematically with the increasing field magnitude. This can be understood because an external field along ⟨001⟩ favors the T phase with the induced polarization along the applied field direction as has been reported by us in an earlier study [32]; as a reference the data are reproduced here (see black lines in Fig. 8). For MD phases, we observe three distinct cases: (1) a comparable

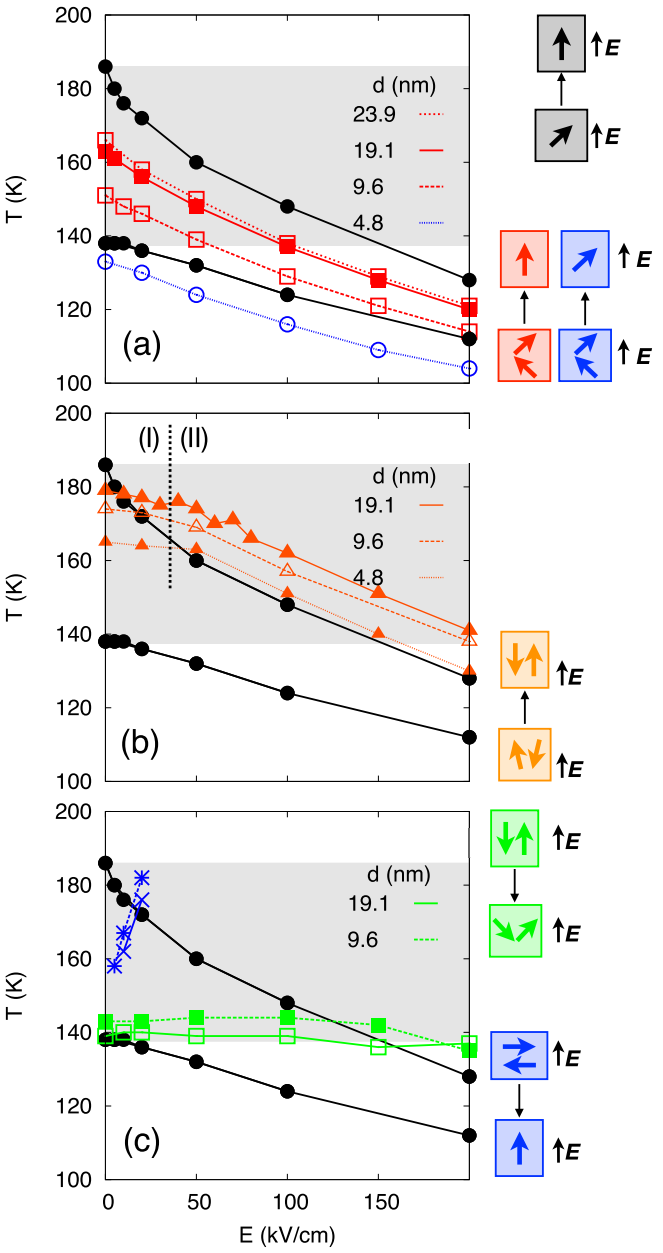

FIG. 8. Change of T ↔ O transition temperatures in the presence of an external field applied along $P_{||}$ (unless mentioned otherwise) for (a) O90, (b) O180, and (c) T180 walls. Gray shaded areas and black lines mark the coexistence region of the SD reference configuration without and with field taken from Ref. [32], respectively. Line types refer to different domain distances (see legends) and colors characterize the phase transitions as follows: red, O90 to T-SD; orange, O180 to T180; green, T180 to O90; whereas in blue, T_t is shown (O90 to O-SD, T180 to T-SD). Each type of transition is shown schematically in the insets. (b) Vertical dashed line marks field range (I) small slope of $T_C(E)$ and (II) larger $T_C(E)$. (c) Blue stars and crosses indicate the transition temperatures when the field is applied perpendicular to the wall.

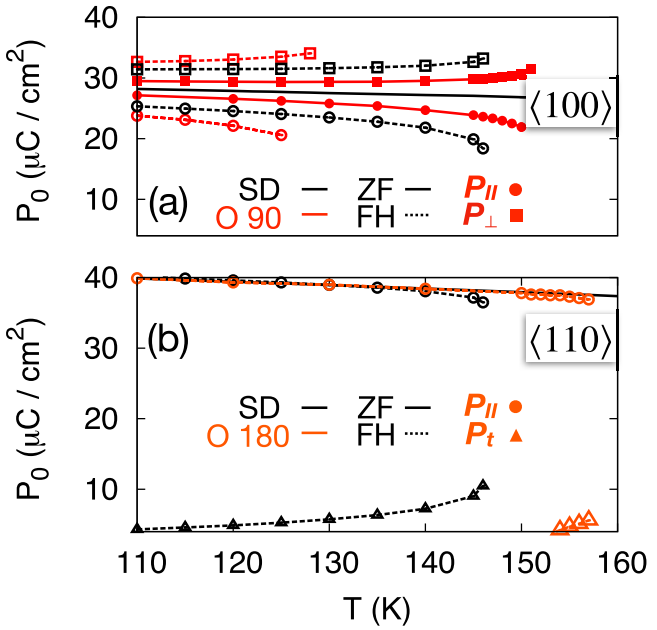

FIG. 9. Monoclinic distortions in domain centers for a field of 100 kV/cm in the presence of (a) O90 and (b) O180 walls (with $d = 9.6$ nm). For reference, the same projections are added for SD phase (black) and zero field (solid lines). The field induces larger monoclinic distortions for O90 walls [$P_\perp$ (squares) > $P_{||}$ (circles)] compared to both zero field phase as well as SD phase under the same field. For O180 walls, the field induces a polarization component P_t (triangles) along the direction which is orthogonal to both $P_{||}$ and $P_\perp$ only for large applied fields and this distortion is smaller compared to the SD phase.

change in T_c with E similar to that found for SD phases for O90 walls [Fig. 8(a)] and O180 walls [region II in Fig. 8(b)]; (2) no or a very small change in T_C with increasing field strength for O180 walls [region I in Fig. 8(b)] and for T180 walls [Fig. 8(c), green squares]; and (3) the reduction in the stability range of dense O90 walls and T180 walls with E [blue symbols in Figs. 8(a) and 8(c), respectively], i.e., $T_t(E)$ increases in cooling simulations and decreases in heating simulations.

Let us now look at the T_C trends for MD configurations in more detail: For O90 walls shown in Fig. 8(a), all domains have the polarization component $P_\perp$ along the applied field direction which results in the partial rotation of dipoles towards the field direction throughout the system and finally the SD T phase parallel to the field. The applied field has a similar impact on the polarization direction as the O90 walls and further enhances the monoclinic distortion with $P_a > P_b$ for the [100] field. These field-induced distortions are larger close to T_C as shown in Fig. 9(a). The field also broadens the DW (not shown); these two effects add up and T_C is reduced with increasing field (case 1).

For the densest walls ($d = 4.8$ nm), the O90 configuration is metastable near the phase transition even in the absence of an external field. The field-induced enhanced monoclinic distortions reduce T_t systematically with field strength thus reducing the stability range of the O90 phase (case 3).

The coupling of O180 walls transforming to T180 with the field shown in Fig. 8(b) is more complex and interesting because the field is neither fully aligned with initial or final polarization nor do all domains incline at the same angle with E and we observe two different field ranges:

(I) For small fields along [010] ($E \leqslant 30\,\mathrm{kV/cm}$), the polarization along $+a+b/-a-b$ transforms to the T180 phases with $+a/-a$, i.e., perpendicular to the field. Here, we observe neither a broadening of the domain wall nor a rotation of P towards the field direction and T_C shows a small dependence on applied field (case 2).

(II) For larger fields along [010], we observe a rotation of the dipoles in both domains to a state with monoclinic distortion and $|P_b| > |P_a|$ promoting the transition to the $+b/-b$ phase collinear with the external field and the slope of $T_C(E)$ matching to that of the SD phase (case 1).

These differences can be related to the field-induced monoclinic distortions. Without field O180 walls do not induce any monoclinic distortion. In field range (I) we observe a reduction of the polarization component antiparallel to the field; i.e., for a field along [010], the $-b$ component in the $-a-b$ domain is reduced. Mediated by the strain the perpendicular tetragonal direction is thus stabilized. Thus, the field neither considerably reduces the energy barrier for the phase transition nor does it stabilize the final state (as P in each domain is perpendicular to the field) and in turn T_C is not lowered by the field. The interesting consequence of this is that the transition temperatures fall outside of the coexistence region of the SD phase with field. In contrast, higher fields [field range (II)] overcome the energy barrier for a monoclinic distortion close to T_C [see polarization component P_t in Fig. 9(b)]. Analogous to the SD case, the distortion promotes the phase transition and we obtain a similar slope of $T_C(E)$ for MD and SD configurations in this field range.

For T180 walls [Fig. 8(c)], the response for the field applied collinear to $P_{||}$ is similar to that observed for O180 walls with small fields (case 2) and again can be understood by a reduced field coupling. The applied field would favor the parallel SD tetragonal phase. However, it is not strong enough to eliminate the walls. Instead the T180 domains with $\pm b$ transform to O90 domains with $\pm bc$. In both phases the field is parallel to $P_{||}$ in one domain and would favor an increase of it, and by the strong strain-polarization coupling, also of the tetragonal strain. The effect of the field is opposite in the other domain, reducing polarization and strain. Such a mismatch at the wall is unfavorable and thus the field coupling is compensated in both phases and T_C is barely modified with field magnitude.

One would expect an anisotropic response to the applied field due to presence of DWs. The complete study of the anisotropy of the field is out of scope in this paper and we focus on one relative direction between field and domain wall for each type of wall. As an example, however, we applied $E_\perp$ to a T180 configuration and the corresponding results are shown in blue in Fig. 8(c). Here, the applied field is perpendicular to polarization in both domains. In this case the energy barrier for rotating the dipoles uniformly towards the field direction is small and further decreases as the system approaches T_C. Therefore, the walls easily disappear and the system transforms to the T-SD phase at T_t which increases with the field magnitude. To sum up, the field coupling depends crucially on the relative direction of field and local polarization in the domains and in particular the combination of elastic walls and electric field along $P_\perp$ leads to a considerable reduction in thermal hysteresis and may thus allow for large reversible functional responses.

IV. SUMMARY AND OUTLOOK

We conducted a systematic study of the coupling of phase transition, domain walls, and electrical field based on molecular dynamics simulations of an *ab initio* effective Hamiltonian. Starting from the idealized bulk $BaTiO_3$ system, we introduced low-energy MD configurations in the orthorhombic and tetragonal phases which are commonly found as complex superstructures in experiments in order to separately discuss their impact on the phase transition.

Thereby we could show that these MD states once nucleated or initialized in the system remain metastable within a temperature range of interest, down to domain width of 4.8 nm. Our observations point to the fact that the monoclinic symmetry observed close to the O-T transition in experiments [7] may be related to elastic domain walls present in the system. Another important consequence of our findings is that the large spread observed in the experimental transition temperatures can be partly related to different domain structures in the sample with no or mainly 180° walls resulting in a broad hysteresis, while elastic walls may induce a monoclinic bridging phase.

Our most exciting finding is that elastic domain walls strongly modify the transition temperatures and reduce the thermal hysteresis by one order of magnitude. On the other hand, the impact of 180° walls is small. These trends are further amplified in the presence of an external field. The combination of external field and O90 walls allows to efficiently push T_C below the zero-field coexistence range which is needed for a large reversible functional response. In contrast, 180° walls reduce the coupling between T_C and the external field and as a result enhance the thermal hysteresis in the presence of an external field compared to the SD case. We have shown that these different trends can be attributed to (1) volume effects, that is, monoclinic distortions within domains, and (2) interface effects, that is, large and diverging DW widths.

Our results are a significant finding for prospective applications using domain wall engineering to reduce thermal hysteresis of the ferroelectric-to-ferroelectric transition. Elastic domain walls may act as a bias to reduce the field strength needed to induce a complete transition in the system and thus yielding large functional responses. This reduction of thermal hysteresis combined with the enhanced piezoelectric response obtained for these systems [20] make domain wall engineered materials especially attractive for applications such as solid-state cooling, which require large response near room temperature. With advanced and precise techniques available to control the growth of nanoferroelectrics [59], we believe that our work would provide a practical guide for further development of functional devices.

ACKNOWLEDGMENTS

A.G. would like to acknowledge financial support by the Deutsche Forschungsgemeinschaft (German research foundation Grants No. GR 4792/1-2 and No.

GR 4792/2) and computational resources provided by the Center for Computational Science and Simulation (CCSS), University of Duisburg-Essen. M.M. would like to acknowledge the funding from the European Union's Horizon 2020 research and innovation programme under Marie Skłodowska-Curie Grant Agreement No. 665919.

[1] J. F. Scott, Science **315**, 954 (2007).
[2] M. Acosta, N. Novak, V. Rojas, S. Patel, R. Vaish, J. Koruza, G. A. Rossetti, Jr., and J. Rödel, Appl. Phys. Rev. **4**, 041305 (2017).
[3] M. E. Lines and A. M. Glass, *Principles and Applications of Ferroelectrics and Related Materials* (Oxford University Press, New York, 1977).
[4] T. Limboeck and E. Soergel, Appl. Phys. Lett. **105**, 152901 (2014).
[5] A. von Hippel, Rev. Mod. Phys. **22**, 221 (1950).
[6] J. Döring, L. M. Eng, and S. C. Kehr, J. Appl. Phys. **120**, 084103 (2016).
[7] C. Eisenschmidt, H. T. Langhammer, R. Steinhausen, and G. Schmidt, Ferroelectrics **432**, 103 (2012).
[8] A. Hershkovitz, F. Johann, M. Barzilay, A. Hendler Avidor, and Y. Ivry, Acta Mater. **187**, 186 (2020).
[9] A. K. Kalyani, D. K. Khatua, B. Loukya, R. Datta, A. N. Fitch, A. Senyshyn, and R. Ranjan, Phys. Rev. B **91**, 104104 (2015).
[10] H. Cao, C. P. Devreugd, W. Ge, J. Li, D. Viehland, H. Luo, and X. Zhao, Appl. Phys. Lett. **94**, 032901 (2009).
[11] T. T. Lummen, Y. Gu, J. Wang, S. Lei, F. Xue, A. Kumar, A. T. Barnes, E. Barnes, S. Denev, A. Belianinov, M. Holt, A. N. Morozovska, S. V. K. L.-Q. Chen, and V. Gopalan, Nat. Commun. **5**, 3172 (2014).
[12] R. Guo, L. E. Cross, S.-E. Park, B. Noheda, D. E. Cox, and G. Shirane, Phys. Rev. Lett. **84**, 5423 (2000).
[13] H. Fu and R. E. Cohen, Nature **403**, 281 (2000).
[14] Y. Bai, X. Han, K. Ding, and L. Qiao, Energy Technol. **5**, 703 (2017).
[15] M. Marathe, C. Ederer, and A. Grünebohm, Phys. Status Solidi B **255**, 1700308 (2018).
[16] E. Stern-Taulats, P. Lloveras, M. Barrio, E. Defay, M. Egilmez, A. Planes, J.-L. Tamarit, L. Mañosa, N. D. Mathur, and X. Moya, APL Mater. **4**, 091102 (2016).
[17] A. Pramanick, A. D. Prewitt, J. S. Forrester, and J. L. Jones, Crit. Rev. Solid State Mater. Sci. **37**, 243 (2012).
[18] J. Fousek and L. E. Cross, Ferroelectrics **293**, 43 (2003).
[19] L. Martin and M. Rappe, Nat. Rev. Mater. **2**, 16087 (2016).
[20] S. Wada, K. Yako, H. Kakemota, T. Tsumuri, and T. Kiguchi, J. Appl. Phys. **98**, 014109 (2005).
[21] W.-F. Rao and Y. U. Wang, Appl. Phys. Lett. **90**, 041915 (2007).
[22] J. Hlinka, P. Ondrejkovic, and P. Marton, Nanotechnology **20**, 105709 (2009).
[23] A. Grünebohm, M. Marathe, and C. Ederer, Appl. Phys. Lett. **107**, 102901 (2015).
[24] X. Ren, Nat. Mater. **3**, 91 (2004).
[25] S. V. Kalinin, Y. Kim, D. D. Fong, and A. N. Morozovska, Rep. Prog. Phys. **81**, 036502 (2018).
[26] V. Y. Topolov, *Heterogeneous Ferroelectric Solid Solutions* (Springer, Berlin, 2018).
[27] A. Grünebohm, M. E. Gruner, and P. Entel, Ferroelectrics **426**, 21 (2012).
[28] J. Padilla, W. Zhong, and D. Vanderbilt, Phys. Rev. B **53**, R5969(R) (1996).
[29] P. Marton, I. Rychetsky, and J. Hlinka, Phys. Rev. B **81**, 144125 (2010).
[30] J. Hlinka, V. Stepkova, P. Marton, and P. Ondrejkovic, in *Topological Structures in Ferroic Materials* (Springer, Cham, 2016), pp. 161–180.
[31] A. J. Bell, J. Appl. Phys. **89**, 3907 (2001).
[32] M. Marathe, D. Renggli, M. Sanlialp, M. O. Karabasov, V. V. Shvartsman, D. C. Lupascu, A. Grünebohm, and C. Ederer, Phys. Rev. B **96**, 014102 (2017).
[33] W. N. Lawless, Phys. Rev. **175**, 619 (1968).
[34] X. Moya, S. Kar-Narayan, and N. D. Mathur, Nat. Mater. **13**, 439 (2014).
[35] A. Grünebohm, Y.-B. Ma, M. Marathe, B.-X. Xu, K. Albe, C. Kalcher, K.-C. Meyer, V. V. Shvartsman, D. C. Lupascu, and C. Ederer, Energy Technol. **6**, 1491 (2018).
[36] W. Zhong, D. Vanderbilt, and K. M. Rabe, Phys. Rev. B **52**, 6301 (1995).
[37] W. Zhong, D. Vanderbilt, and K. M. Rabe, Phys. Rev. Lett. **73**, 1861 (1994).
[38] T. Nishimatsu, A. Grünebohm, U. Waghmare, and M. Kubo, J. Phys. Soc. Jpn. **85**, 114714 (2016).
[39] I. A. Kornev, L. Bellaiche, P.-E. Janolin, B. Dkhil, and E. Suard, Phys. Rev. Lett. **97**, 157601 (2006).
[40] J. Paul, T. Nishimatsu, Y. Kawazoe, and U. V. Waghmare, Phys. Rev. Lett. **99**, 077601 (2007).
[41] B.-K. Lai, I. Ponomareva, I. A. Kornev, L. Bellaiche, and G. J. Salamo, Phys. Rev. B **75**, 085412 (2007).
[42] M. Marathe, A. Grünebohm, T. Nishimatsu, P. Entel, and C. Ederer, Phys. Rev. B **93**, 054110 (2016).
[43] I. Ponomareva and S. Lisenkov, Phys. Rev. Lett. **108**, 167604 (2012).
[44] Z. Gui, S. Prosandeev, and L. Bellaiche, Phys. Rev. B **84**, 214112 (2011).
[45] T. Nishimatsu, M. Iwamoto, Y. Kawazoe, and U. V. Waghmare, Phys. Rev. B **82**, 134106 (2010).
[46] http://loto.sourceforge.net/feram/.
[47] T. Nishimatsu, U. V. Waghmare, Y. Kawazoe, and D. Vanderbilt, Phys. Rev. B **78**, 104104 (2008).
[48] S. D. Bond, B. J. Leimkuhler, and B. B. Laird, J. Comput. Phys. **151**, 114 (1999).
[49] We occasionally observe nucleation of domains during cooling or heating simulations especially around the transition temperatures for fast temperature sweeps. For the chosen simulation time and sweep rate, we do not observe a transformation from the MD to SD phase apart from the phase transition.
[50] Note that the multidomain states are only (meta)stable above a critical minimal distance and hence systems with denser walls transform to the corresponding SD state at specific temperatures T_i; these systems are excluded from the introductory discussion.
[51] J. Hlinka and P. Márton, Phys. Rev. B **74**, 104104 (2006).
[52] B. Meyer and D. Vanderbilt, Phys. Rev. B **65**, 104111 (2002).

[53] Y.-H. Shin, I. Grinberg, I. Chen, and M. Rappe, Nature **449**, 881 (2007).

[54] Note that domain walls occasionally move and the domain wall distances are no longer equidistant. However, for simplicity, we name the MD configurations following the initial domain distances.

[55] Recall that unfortunately due to computational restrictions we have not performed a systematic study for this type of wall.

[56] G. A. Rossetti and A. G. Khachaturyan, Appl. Phys. Lett. **91**, 072909 (2007).

[57] M. Acosta, N. Khakpash, T. Someya, N. Novak, W. Jo, H. Nagata, G. A. Rossetti, and J. Rödel, Phys. Rev. B **91**, 104108 (2015).

[58] Our chosen field direction ⟨100⟩ put certain limits on the studied cases. For example, for T90 walls, the domains wall is parallel to the ⟨110⟩ direction; therefore, these walls are not included in this study of wall-field coupling.

[59] A. Schilling, D. Byrne, G. Catalan, K. G. Webber, Y. A. Genenko, G. S. Wu, J. F. Scott, and J. M. Gregg, Nano Lett. **9**, 3359 (2009).